Barotropic Instability and Equatorial Superrotation

G. P. WILLIAMS

NOAA/Geophysical Fluid Dynamics Laboratory, Princeton University, Princeton, New Jersey

ABSTRACT

Baroclinically unstable zones in midlatitudes normally produce medium-scale planetary waves that propagate toward the equator where they generate easterlies while transferring westerly momentum poleward, so that the jet lies in higher latitudes than in the corresponding axisymmetric (eddy-free) state. When the baroclinically unstable zone is moved into low latitudes, however, the equatorward side of the jet can also produce a barotropic instability whose large-scale eddies lead to a strong superrotating westerly current at the equator; the jet remains close to its axisymmetric location. For the earth, the transition between these two regimes occurs when the jet lies close to 30°, according to calculations with a global, multilevel, spectral, primitive equation model that examines superrotating flows for a wide range of rotation rates. The existence of a stable superrotating regime implies that an alternative climate could occur, but only under novel conditions.

1. Introduction

Westerly winds rarely occur at the equator in the earth's troposphere, least of all near the surface. But they can arise in two-level primitive equation models when the system is subjected to an additional low-wave-number forcing in the Tropics (Suarez and Duffy 1992; Saravanan 1993). In such a model atmosphere, the equatorial westerlies tend to be long lived but their persistence appears to be resolution dependent if the forcing is removed. Equatorial westerlies also occur in moist and dry general circulation models (GCMs), particularly in those with low rotation rates (Williams 1988), where they coexist with midlatitude westerlies; they also occur in the Jovian atmospheres, where they coexist with multiple jets.

Here, we show how equatorial westerlies can be generated simply and consistently by the instability of a jet lying in low latitudes. The behavior of jets lying in midlatitudes is well known: their characteristic poleward eddy momentum flux is due to neutral planetary waves propagating equatorward aloft after being generated by a baroclinic instability near the surface—see Held and Hoskins (1985) for a synopsis of the process and the theory. On the other hand, the behavior of low-latitude[1]

---

[1] The distinction between "low" and "mid" latitudes becomes less meaningful at lower rotation rates.

Corresponding author address: Dr. G. P. Williams, NOAA/GFDL, Princeton University, P.O. Box 308, Princeton, NJ 08542-0308.
E-mail: gw@gfdl.noaa.gov

jets has been less studied, presumably because they are less likely to occur under the existing terrestrial conditions.

The low-latitude jets are developed numerically using a global, multilevel, spectral, primitive equation model subject to a simple Newtonian heating function. In classifying the resulting solutions, the flow is defined as being in the *superrotating* state or regime when the instability of the jet leads to a significant long-lived westerly at the equator; otherwise, the flow is considered to be in the *classical* state or regime when the equator has easterlies or weak westerlies. Occasionally the system exhibits a *transitory* state when significant but short-lived westerlies arise at the equator. For brevity and clarity, the main jet and equatorial current are sometimes referred to using the W_1 and W_0 symbols, respectively.

The presentation begins in section 2 with a brief discussion of the numerical model and parameters. This is followed in section 3 by a mapping of the regimes for a wide range of rotation rates, together with details of two solutions that illustrate the two basic states that occur when the baroclinicity is relocated from middle to low latitudes for the normal rotation rate. Then, in section 4, the solutions for other rotation rates are documented in detail to examine the variability of the superrotating regime as the eddy scales alter. The effect of the stratosphere on superrotation is also explored briefly. Finally, the eddy processes that drive the superrotation are analyzed in section 5 using the Eliassen–Palm flux and potential vorticity gradient.

TABLE 1. The basic heating parameters for the functions defined in (2) and (3) for the cases presented. The parameter Ω^* denotes the rotation rate relative to the standard value. The resolution denotes the rhomboidal truncation wavenumber (R) and the number of vertical levels (L). For the R63 resolution, the transform grid spacings are $\Delta\lambda \approx 2°$ and $\Delta\phi \approx 1°$. The parameter n denotes the power of $\cos^n\phi$ in the heating profile. The heating and drag rates are fixed at $\tau = 20$ days and $\tau_d = 1$ day. The Time column gives the extent of each calculation in days. The zonal velocities, Umax and Ueq, give the maximum jet and equatorial flow values at the end of the calculation (m s^{-1}), while Ulat gives the latitude of the mean jet core aloft. The biharmonic diffusion coefficient ν_4 equals $-(0.5, 0.1, 0.05) \times 10^{16}$ m^4 s^{-1} for the R(30, 42, 63) resolutions, respectively. The stratospheric temperature T_s equals 200 K, except for the B2 case, where no stratosphere is imposed. The surface boundary layer extends to the $\sigma_b = 0.8$ level in all cases, even though Ekman layer theory suggests that the layer be made thicker as Ω^* decreases.

Case	Ω^*	n	Δ	δ	Resolution	Time	Umax	Ueq	Ulat
A	1	4	0.2	0.1	R30L30	500	57	-4	45°
B	1	16	0.1	0.1	R42L30	1000	67	30	23°
B2	1	16	0.1	0.1	R42L30	1000	58	53	24°
C	4	64	0.1	0.1	R63L30	500	67	42	12°
D	2	32	0.1	0.1	R63L30	500	63	36	17°
E	1/2	8	0.1	0.1	R30L30	1000	61	24	32°
F	1/4	4	0.1	0.1	R30L30	2000	74	42	43°
G	1/8	2	0.1	0.1	R30L30	1500	75	55	52°

2. Numerical model

a. System of equations

The numerical model is based on the dynamical core of the Geophysical Fluid Dynamics Laboratory spectral GCM and is driven by a simple heating function, along the lines discussed by Held and Suarez (1994). The primitive equations have the standard hydrostatic, vorticity–divergence form that is preferred for the semiimplicit, spectral transform scheme devised by Bourke (1974); these are summarized, for example, in Gordon and Stern (1982), and in section 2.1 of Williams (1988). The model predicts the zonal, meridional, and vertical velocity components (u, v, ω), plus the temperature and surface pressure fields (T, p_*), as a function of the latitude, longitude, and sigma vertical coordinates (ϕ, λ, σ), where $\sigma = p/p_*$ is the normalized pressure. The variable $\psi(\phi, \sigma) = -\int \overline{v} \cos\phi \, d\sigma$ defines a quasi streamfunction for the zonally averaged meridional motion.

As well as a heating function, the equations include biharmonic diffusion terms in the horizontal and, in the vertical, a linear boundary layer drag of the form

$$\frac{\partial(u, v)}{\partial t} \cdots = -\frac{(u, v)}{\tau_d} \max\left(0, \frac{\sigma - \sigma_b}{1 - \sigma_b}\right), \quad (1)$$

where τ_d and σ_b define the timescale and the extent of the mixing. Topography, moisture, vertical diffusion, and convective adjustment are all omitted. The numerical procedure uses a rhomboidal truncation at wavenumber 30, 42, or 63 in the horizontal, with 30 equally spaced σ levels in the vertical. Table 1 lists the main parameter values.

b. Heating function

All flows are developed from an isothermal state of rest and are maintained by a Newtonian heating function of the form

$$\frac{\partial T}{\partial t} \cdots = \frac{(T_r - T)}{\tau}, \quad (2)$$

where the heating rate is proportional to the difference between the atmospheric temperature and a specified radiative–convective temperature $T_r(\phi, \sigma)$, and is dependent upon a radiative–convective damping time $\tau(\phi, \sigma)$, which is set to a constant. The following distribution

$$T_r(\phi, \sigma) = \max\{T_0\sigma^\kappa[1 + \Delta P(\phi) + \delta F(\sigma)], T_s\}, \quad (3)$$

provides the heating, where T_0 and T_s are tropospheric and stratospheric reference temperatures. The constants Δ and δ define the amplitude of the horizontal and vertical potential temperature gradients. The functional forms are not critical and are chosen for simplicity, with $F = (1 - \sigma^\kappa)/\kappa$ providing a fairly constant static stability and Brunt–Väisälä frequency $N = (g\theta_z/\theta)^{1/2}$ in the troposphere, where $\theta = T\sigma^{-\kappa}$ is the potential temperature and κ is a gas ratio (see below). This $F(\sigma)$ closely matches the standard $\log\sigma$ distribution used by Held and Suarez (1994) but remains finite at the upper boundary.

The baroclinicity provided by the $P(\phi)$ function is normally based on the second Legendre polynomial or on $\cos^2\phi$, so to examine jets in lower latitudes it is convenient to represent the heating by the form $\cos^n\phi$, where n varies from 2 to 64, as shown in Fig. 1. Heating functions with high n values should not be regarded as extreme but merely as a simple way of confining the baroclinicity to lower latitudes; the same effect could be achieved by using simple linear representations. Physically, the defining parameter is the baroclinicity center ϕ^c, which corresponds to the inflexion point in the $\cos^n\phi$ distributions and is given by the relation $\tan^2\phi^c = (n - 1)^{-1}$.

c. Parameter values

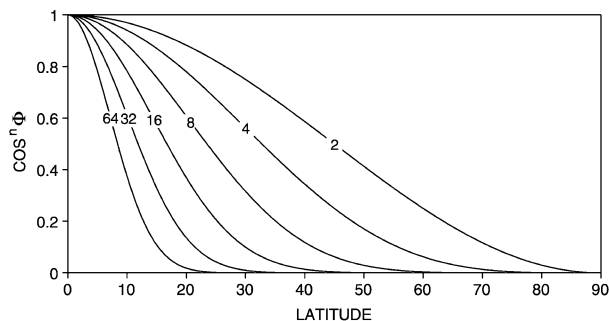The fixed physical parameters needed in the calculations use the following standard values: $a = 6370 \times$

FIG. 1. The latitudinal heating profile $\cos^n\phi$ shown for various values of n. The baroclinicity centers or inflexion points ϕ^c lie at the n labels.

10^3 m and $\Omega = 7.292 \times 10^{-5}$ s^{-1} for the planetary radius and rotation rate; $g = 9.8$ m s^{-2} for the acceleration of gravity; $c_p = 1004$ J kg^{-1} K^{-1} for the specific heat of air; $\kappa \equiv R/c_p = 2/7$, where R is the gas constant; $p_0 = 1000$ mb for a mean surface pressure based on the total mass p_0/g; and $T_0 = 288$ K for the initial temperature.

In presenting the solutions, the figures use solid contour lines to plot positive and zero values, while dashed lines denote negative values. The zero-value contours are omitted from many plots for clarity. Most fields shown are time-averaged quantities, based on zonal means sampled twice a day from the onset of the baroclinic instability (usually at 100 ± 20 days) to the end of the calculation (see Table 1). For many of the spectra and cospectra, the contour intervals are not uniform but, rather, the contour values are based on powers of two so as to expose the weaker but vital contributions near the equator.

d. Analysis functions

The solutions are described using standard analysis procedures and notation, with the overbar and prime denoting the zonal mean and eddies. The power spectrum for u' and the covariance spectrum for u' and v' in longitudinal wavenumber k are calculated as a function of altitude and latitude, using Parseval's theorem—see section A3 of Peixoto and Oort (1992).

The Eliassen–Palm flux vector $\mathbf{F} = \{F^{(\phi)}, F^{(p)}\}$ and flux divergence E are defined following Andrews and McIntyre (1978) and Edmon et al. (1980) as

$$F^{(\phi)} = \left(-\overline{u'v'} + \overline{u}_p \frac{\overline{v'\theta'}}{\overline{\theta}_p}\right) \frac{\cos^2\phi}{a}, \tag{4}$$

$$F^{(p)} = \left((f + \overline{\zeta}) \frac{\overline{v'\theta'}}{\overline{\theta}_p} - \overline{\omega'u'}\right) \cos^2\phi, \tag{5}$$

$$E = \frac{\partial F^{(\phi)}}{\partial \phi} + \frac{\partial F^{(p)}}{\partial p}, \tag{6}$$

where $f = 2\Omega \sin\phi$ and $\overline{\zeta} = -(a \cos\phi)^{-1}(\overline{u} \cos\phi)_\phi$.

The first terms in (4) and (5) are the dominant geostrophic components and are denoted as $F^{(\phi g)}$ and $F^{(pg)}$, while the third term in (5) is found to be the dominant ageostrophic term near the equator and is referred to as $F^{(\omega)}$. In plotting the vectors, $F^{(\phi)}$ and $F^{(p)}$ are scaled by one radian of latitude and one pascal of pressure, respectively, to give similar units, and in some cases $F^{(\phi)}$ is also magnified by an empirical factor to make its contribution more apparent.

The mean quasigeostrophic potential vorticity gradient is defined, again following Edmon et al. [1980, Eq. (3.8)], on normalizing by 2Ω, as

$$\overline{q}_\phi = \cos\phi + \frac{\overline{\zeta}_\phi}{2\Omega} + \sin\phi\left(\frac{\overline{\theta}_\phi}{\overline{\theta}_p}\right)_p. \tag{7}$$

For convenience in defining their role in the barotropic and baroclinic instabilities, the first two terms are referred to as the barotropic component $\overline{q}_\phi(\mathrm{BT})$ and the third term as the baroclinic component $\overline{q}_\phi(\mathrm{BC})$.

3. Circulation regimes

Consider first the limits of the classical and superrotating regimes as defined by a set of solutions made for a wide range of rotation rates. These put in perspective the two basic cases, one for each state, whose detailed description then follows.

a. Regime limits

The midlatitude jet and equatorial easterly of the classical atmospheric regime are usually reproduced with the heating parameter n set to 2 or 4. But when $n = 6$–12 a low-latitude jet forms whose instability leads to an equatorial westerly wind that is stronger and longer lasting at the larger n values but is never permanent; eventually the classical regime becomes reestablished with the jet lying in the 30°–40° zone. However, when $n = 16$, the equatorial westerly becomes a permanent feature. We consider the limiting cases with $n = 4$ and $n = 16$ as providing the best representation of the two main regimes at the normal rotation rate, and other cases with $n = 6$–12 as being transitory.

The regime boundaries also depend strongly on the rotation rate. To derive these, solutions are also obtained at slower and faster rotation rates, with $\Omega^* = (1/8, 1/4, 1/2, 2, 4)$, where Ω^* is the rotation rate normalized by the standard value. For simplicity in comparing the solutions, the heating coefficients are kept fixed at $\Delta = 0.1$ and $\delta = 0.1$ for the various n and Ω^* values. Higher horizontal resolutions are used at higher Ω^* because the jets become narrower and the eddies become smaller as the rotation rate increases (see Table 1). The results are summarized in Fig. 2, where the lower curve defines the limits at which strong superrotating westerlies occur and the upper curve defines the limits at which classical flows occur, as a function of ϕ^c and Ω^*. In between the two curves the flows are of a transitory character.
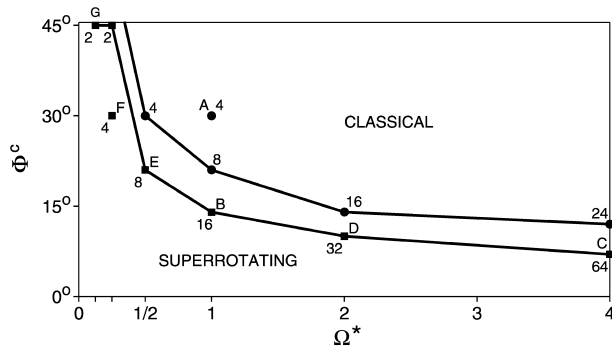
FIG. 2. The separation of the superrotating and classical regimes, as defined by the center of the baroclinic zone ϕ^c and by the relative rotation rate Ω^* for the values of n marked and for the parameters listed in Table 1. The square (round) points denote the main superrotating (classical) cases examined by calculations whose resolution varies only as a function of Ω^*. The labels A–G indicate the cases that are discussed in detail.

The calculations show that strong superrotating states occur for baroclinic zones with $n = (2, 4, 8, 16, 32, 64)$ when $\Omega^* = (1/8, 1/4, 1/2, 1, 2, 4)$, respectively. Note that the quantity n/Ω^* is constant along the boundary defined by these cases. At $\Omega^* = 1/4$, an extra case with $n = 2$ produces only a weak W_0 flow, but this is enough to show that the classical regime cannot exist at this rotation rate. Thus, superrotation is the natural state at low rotation rates. Although these curves are only valid for the parameters selected, they do give some idea of the basic variation and show that the two regimes exist over a wide rotational range. The regime transition has a lesser dependence on the values of Δ and δ, even though the two regimes depend crucially on these parameters for producing and controlling the underlying instabilities.

b. The classical state

The annual mean state of the atmosphere can be reproduced quite realistically with the heating parameters set to $n = 2$, $\Delta = 0.2$, and $\delta = 0.05$. In such a case (not shown), after the initial spinup, the axisymmetric[2] jet at 30° goes unstable and forms a 3D midlatitude jet whose mean location lies close to 55° aloft. To produce flows that match the observed terrestrial state more closely, higher-order refinements in the formulation of the heating function are required to implement the formulae devised by Held and Suarez (1994).

For present purposes, it is convenient to regard the classical circulation to be that produced by a heating profile with $n = 4$ as this yields a jet closer to the observed annual mean location at 45°. The formulation of Held and Suarez (1994) also contains a $\cos^4\phi$ heating

component but it is implemented through the $\tau(\phi, \sigma)$ variation, rather than through the $P(\phi)$ profile. The latitude of the mean jet also depends on the magnitude of τ—which tends to restore the jet toward the axisymmetric location at 30°—and this can increase by about 5° when τ goes from 10 to 40 days. For comparison with other cases, it is also convenient to make the system more statically stable by setting $\delta = 0.1$ in the A case (see Table 1).

In the resulting circulation for case A in Fig. 3, the baroclinic instability, as defined by the eddy heat transport $\overline{v'T'}$, peaks near the surface at 40° and has a secondary maximum near the tropopause. The surface instability acts as the main source of the planetary waves that transport easterly momentum toward the equator. Such wave action gives a poleward $\overline{u'v'}$ flux aloft that helps maintain the mean jet at a latitude that lies 15° poleward of the initial axisymmetric current. The instability also drives the Ferrel cell that occupies the 30°–60° zone, as well as modifying the Hadley cell. The easterly flow in low latitudes helps define this classical state.

The eddy variance of the zonal wind $\overline{u'u'}$ gives another measure of the eddy activity and is strongest within the upper jet. Its components in the $u'^2(k)$ spectrum are distributed throughout zonal wavenumber space in the same way at all levels, and at $\sigma = 0.3$ in Fig. 3d they display two peaks at $k = 4$ on the flanks of the jet at $\phi = 30°$ and 50°, with the poleside component dominating.[3] A third peak occurs at $k = 1$–2 in the center of the jet at 45° latitude. These features match those seen in Fig. 4 of Held and Suarez (1994). The medium-scale ($k = 4$–5) eddies also dominate the $u'v'(k)$ cospectrum in Fig. 3h where they form a large lobe that coincides with the jet's equatorside flank. These eddies all transfer angular momentum poleward to maintain the jet at 45°. But the absence of any contribution at the largest scales implies that the eddies seen at $k = 1$–2 in the $u'^2(k)$ spectrum do not transfer any angular momentum. Similar features are seen in Fig. 6a of Saravanan (1993).

c. The superrotating state

When the center of baroclinicity is moved from the 30° location of the A ($n = 4$) case to the 14° latitude of the B ($n = 16$) case, the flow evolves as in Fig. 4. The instabilities (identified more fully in section 5) set in at 90 days and soon lead to an equatorial westerly flow that grows to 30 m s^{-1} over 200 days but then develops more gradually, equilibrating after about 2 years (see Fig. 4a). Superrotating currents that fail to achieve a substantial amplitude tend to be transitory and usually collapse. In the B case, however, the combined westerly flow persists and eventually produces what looks like a single westerly at the equator (see Fig. 4b). The final jet core lies close to its axisymmetric spinup

---

[2] By "axisymmetric" state, we mean the 2D circulation that exists just prior to the instability onset. Such a circulation closely approximates the equilibrated eddy-free state.

[3] Differences between distributions in the two hemispheres provide a measure of the sampling error in forming the time means.

position, unlike the classical case where it lies significantly poleward of its axisymmetric position.

The basic fields in Fig. 5 are averaged over almost the entire period of the calculation, starting at the onset of the instabilities. Thus the time-mean jet has a weaker W_0 current than does the final flow.[4] The baroclinic instability, as defined by the $\overline{v'T'}$ flux, is relatively shallow, lying mainly below the $\sigma = 0.5$ level, but extending over 5°–45° in latitude, with a peak near the jet axis at 23°. This shallow instability also drives direct and indirect cells that are narrower and shallower than in the classical state.

The eddy momentum flux $\overline{u'v'}$ produced in response to the instabilities is complex, being made up of three components,[5] when the jet lies in low latitudes. The main poleward component coincides with the jet axis but, unlike the classical state, it is also strong in the lower atmosphere (see Fig. 5f). The flux also has an important equatorward component in the upper troposphere on the equatorside of the main lobe; this is responsible for the growth of the W_0 westerly current. Another equatorward flux lies on the poleside of the main lobe and shows that the eddies converge angular momentum into the jet flank. The $\overline{u'u'}$ variance implies that there are two centers of eddy activity, one located within the baroclinic instability at $\sigma = 0.7$, $\phi = 16°$, and another within the jet flank near $\sigma = 0.2$, $\phi = 30°$ (Fig. 5g). There is also a weaker component aloft at the equator itself that reflects the presence of long-lived eddies trapped between the two W_1 jets.

This last component shows up best in the $u'^2(k)$ power spectrum when plotted using contour values based on powers of two to expose the weaker contributions. The resulting field in Fig. 5d reveals the presence of large weak eddies with wavenumbers of $k = 1$–2 at the equator and $k = 1$–4 at the jet axis. Within the W_1 jet, however, the main variance occurs in two peaks, one on each side of the jet axis (as in the A case) and centered on $k = 7$ at all heights, as might be expected for such a regular wavy jet.

Similar scales prevail in the $u'v'(k)$ cospectrum in Fig. 5h, where the main lobe lying in the jet axis is associated with the medium ($k = 5$–8) wavenumbers at $\phi = 30°$. The equatorward flux that drives the W_0 current, however, is confined to low ($k = 1$–2) wavenumbers and to low latitudes ($|\phi| \leq 20°$). The additional poleward flux centered at $k = 3$ and $\phi = 25°$ may reflect the presence of a process that acts as an intermediary between the two main eddy groups.

The wave sources and actions that produce the complex eddy fluxes and the superrotating current in the B case are not obvious. On the other hand, in the classical A case we know that the unstable baroclinic mode at

40° excites the neutral waves that transport easterly momentum equatorward for all phase speeds into wave-breaking regions near critical latitudes in the subtropics. However, in the superrotating B case, the unstable baroclinic mode centered at 23° excites medium-scale waves that appear to disperse both poleward and equatorward to maintain the W_1 jet, while the large modes in low latitudes appear to transfer easterly momentum poleward to form the W_0 current. According to Saravanan's (1993) analysis of the superrotating regime in the two-level, tropical wave model, the high-wavenumber disturbances have turning points near the equator where they are reflected by the strong westerlies and so go poleward. In addition, his low-wavenumber disturbances propagate between the two hemispheres but have no preferred direction. Such processes do not appear to prevail in the superrotating flows under discussion, but the issue is deferred until section 5 when the broader picture presented by flows with a wider range of rotation rates and eddy scales can be assessed.

d. Numerical issues

Although the superrotating state is robust, further calculations show that its onset and form have a modest dependence on the numerical procedure and resolution. In particular, the results described above depend on developing the flow from a state of rest, then proceeding through a near-axisymmetric spinup to the onset of the instabilities and the generation of the W_1 jet and W_0 current. However, if a classical flow is developed first by a heating with $n = 4$ and if this is then used to initialize calculations with $n = 16$, the ensuing broader spectral activity can result in a transitory flow. To progress from a classical state to a superrotating flow comparable to that of the B case then requires either a larger ($n = 32$) or a faster ($\tau = 10$ days) heating parameter. Nevertheless, the present solutions do appear to accurately represent the basic character of the superrotating state, according to additional calculations with a variety of higher horizontal (R84, R126) and vertical (L50) resolutions.

4. Superrotation at other rotation rates

To examine the character of the superrotating regime at faster and slower rotation rates, the C–G solutions for $\Omega^* = (4, 2, 1/2, 1/4, 1/8)$ are documented in Figs. 6 and 7—Table 1 lists the related parameters. Although the superrotating flows for $\Omega^* = 2$ and 4 are essentially just narrower versions of the state at $\Omega^* = 1$, the solutions for $\Omega^* = 1/4$ and 1/8 are not just wider versions of the flow for $\Omega^* = 1$ and 1/2 but, rather, are examples of what happens when the baroclinic instability becomes hemispheric in scale and approaches its cutoff; such cases define the regime's lower limit. The character of superrotating flows also depends to a lesser extent on the relative thickness of the stratosphere and this is examined in section 4c.

---

[4] Recalculating the B case for $n = 64$ gives a flatter profile, with the W_0 and W_1 currents having maxima of 42 and 71 m s⁻¹.

[5] Recalculating the B case for a higher (R84L30) horizontal resolution produces a nearly identical distribution and solution.
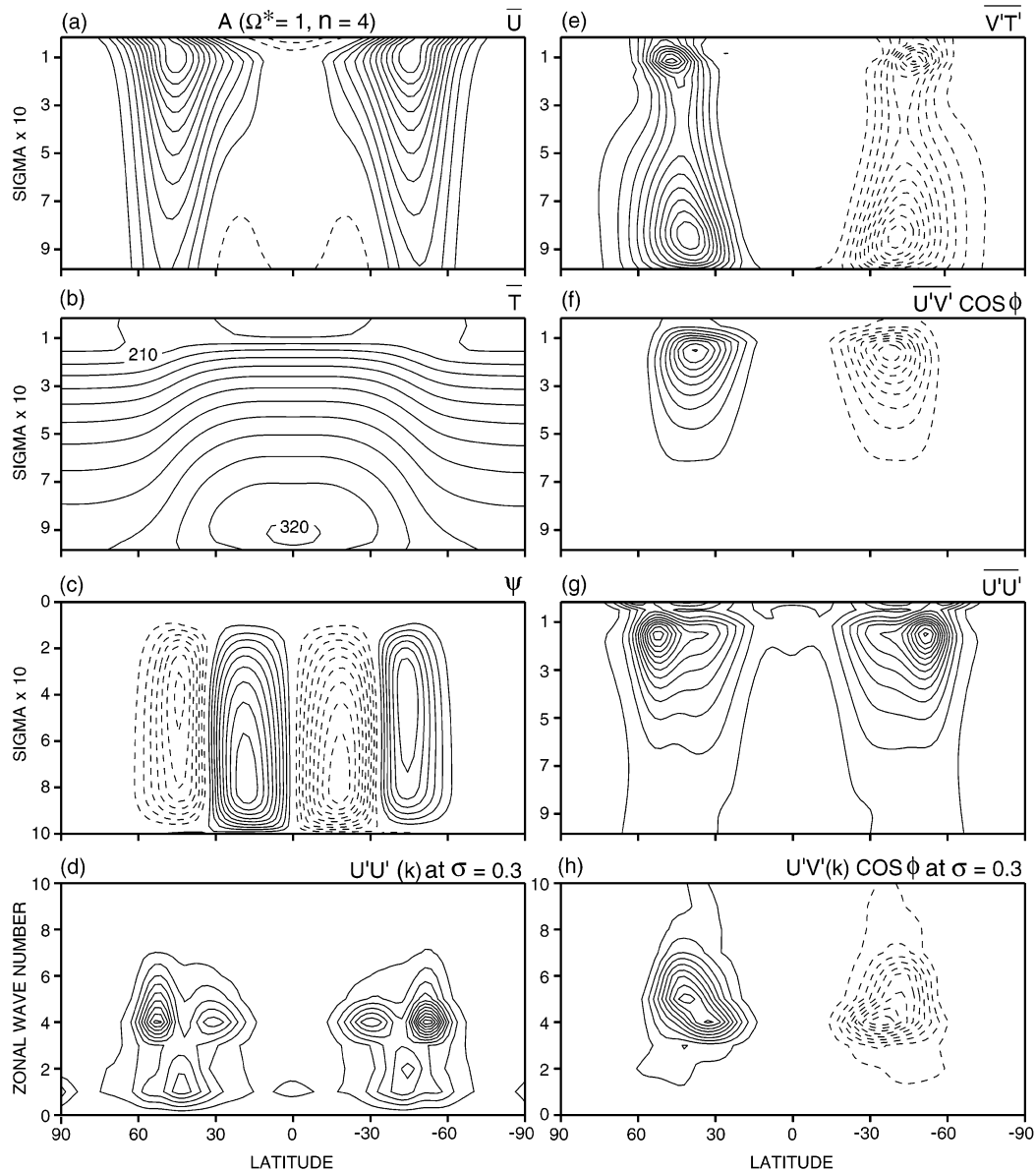
FIG. 3. Meridional sections of the primary mean and eddy fields for the classical A solution with $\Omega^* = 1$ and $n = 4$. Labels at the top of each panel indicate the field depicted. The contour intervals are (a) 5 m s^{-1}, (b) 10 K, (c) 0.02 s^{-1}, (d) 15 m^2 s^{-2}, (e) 2 K m s^{-1}, (f) 10 m^2 s^{-2}, (g) 30 m^2 s^{-2}, and (h) 3 m^2 s^{-2}. The spectra are evaluated at $\sigma = 0.3$. The zero-value contours are omitted and negative values are dashed.

a. Faster rotation

When $\Omega^* = 2$ and 4, the latitudinal flow scales are narrower and, consequently, the heating needs profiles with $n = 32$ and 64 in the two cases to locate the baroclinicity in lower latitudes and thereby produce strong superrotating states. Most fields in the D and C cases, in column 1 of Figs. 6 and 7, are indeed just narrower versions of the basic form, with the baroclinic instability remaining shallow as before. The $\overline{u'v'}$ fluxes are again complex and again suggest that neutral waves propagate in both directions out of the jet axis, thereby

converging momentum into the jet core—such transports resemble those occurring in the multiple midlatitude jets produced by GCMs with high rotation rates (Williams 1988).

The $u'^2(k)$ power spectra also have the same form as that at $\Omega^* = 1$, but with the main eddy activity centered at higher wavenumbers, at $k = 10$ and 15 for $\Omega^* = 2$ and 4, respectively. The weaker eddy activity near the equator, however, is spread over a wider range of low wavenumbers, over $k = 1$–5 and 1–7 in the two cases (Figs. 6g1 and 7g1). Likewise, the $u'v'(k)$ cospectra consist of the same three subgroups as at $\Omega^* = 1$, but
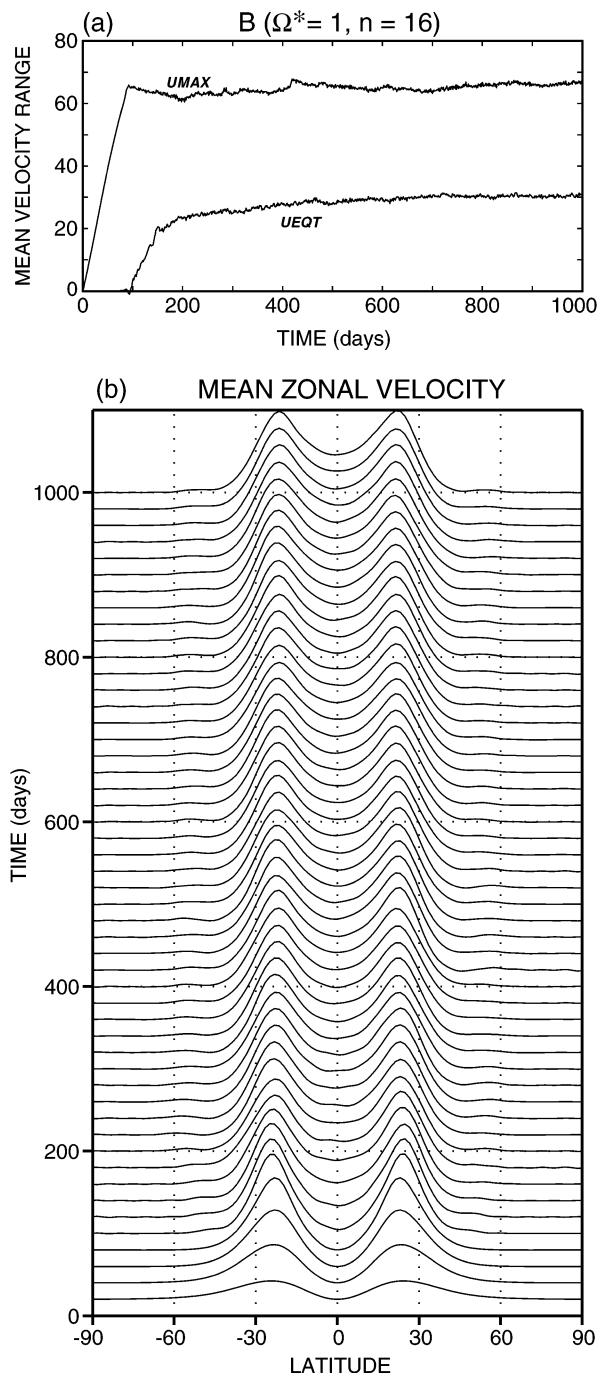
FIG. 4. Diagnostic transients for the superrotating B solution show (a) the evolution of the maximum westerly flow in low latitudes (UMAX for the W_1 jet) and at the equator (UEQT for the W_0 current; m s^{-1}), and (b) the time sections of the mean zonal velocity, sampled near the tropopause. The scale for the maximum $\overline{u}$ is 68 m s^{-1} and is equivalent to five times the vertical increment.

Although the intermediary wavenumber group is less distinct when $\Omega^* = 4$, the overall impression is that the same eddy processes are involved for all cases between $\Omega^* = 1$ and 4—only the eddy scales differ.

b. Slower rotation

At slower rotation rates the superrotating regime flourishes, with the ratio of the W_0 to W_1 amplitudes increasing over the $\Omega^* = 1/2$ to 1/8 range (Table 1). The scale of the superrotating flow fields also increases over this range, becoming so wide that the eddy fluxes have to change their character for the E–G cases in Fig. 6. The peak wavenumber in the $u'^2(k)$ spectra drops from 7 to 4 to 3 to 1 when Ω^* decreases from 1 to 1/2 to 1/4 to 1/8, in keeping with the increasing scale of the baroclinic instability (Figs. 6g). However, in the limit, when $\Omega^* = 1/16$, the baroclinic instability almost becomes extinct and the superrotating state weakens.[6]

When Ω^* drops to half the normal value, as in the E ($n = 8$) case, the main changes—apart from the wider scale—occur in the $\overline{u'v'}$ flux, which becomes simpler by losing the poleside equatorward component, and thus becomes more clearly split into a poleward component that slopes along the W_1 jet axis and a weaker inner equatorward component that drives the W_0 current. Decreasing Ω^* further to 1/4 and 1/8 makes superrotation the natural state and completely excludes the classical regime before the baroclinic instability limit is reached. Now, the jets slope more to peak aloft on the poleward edge of the direct cells, at 43° and 52° in the F ($n = 4$) and G ($n = 2$) cases in Fig. 6. A strong deep equatorial westerly prevails in both cases, even more so in the G case where the W_0 and W_1 currents define a flatter jet profile than in any other case. Although the indirect cell barely exists in the G case, it still coincides with the center of the now hemispheric-scale baroclinic instability. This instability, however, remains below the $\sigma = 0.5$ level, just as it does for all superrotating flows at all Ω^*.

As Ω^* decreases in this range, the eddies produce a stronger equatorward $\overline{u'v'}$ flux that approaches the poleward flux in amplitude and scale in the F case, and in the G case actually becomes dominant, with the poleward flank of the jet acting as the the main source of the eddy energy, according to the $\overline{u'u'}$ variance. Unlike the other cases, the variance components merge vertically into a single lobe in the jet flank and imply that only a single eddy source exists in higher latitudes.

Comparing the various superrotating solutions, over the $\Omega^* = 1/8$ to 4 range, shows that the regime exhibits many features in common, but has a variety of eddy momentum flux forms. This diversity may help us iso-

with each located at higher wavenumbers as Ω^* increases. The vital low-wavenumber fluxes that transport angular momentum toward the equator now occur at $k = 1–4$ and 1–8 in the two cases (Figs. 6h1 and 7h1).

---

[6] Dry and moist GCMs with realistic radiative heating also have their strongest and deepest equatorial westerly when $\Omega^* = 1/4$, and a baroclinic instability that vanishes when $\Omega^* = 1/16$ (Williams 1988).
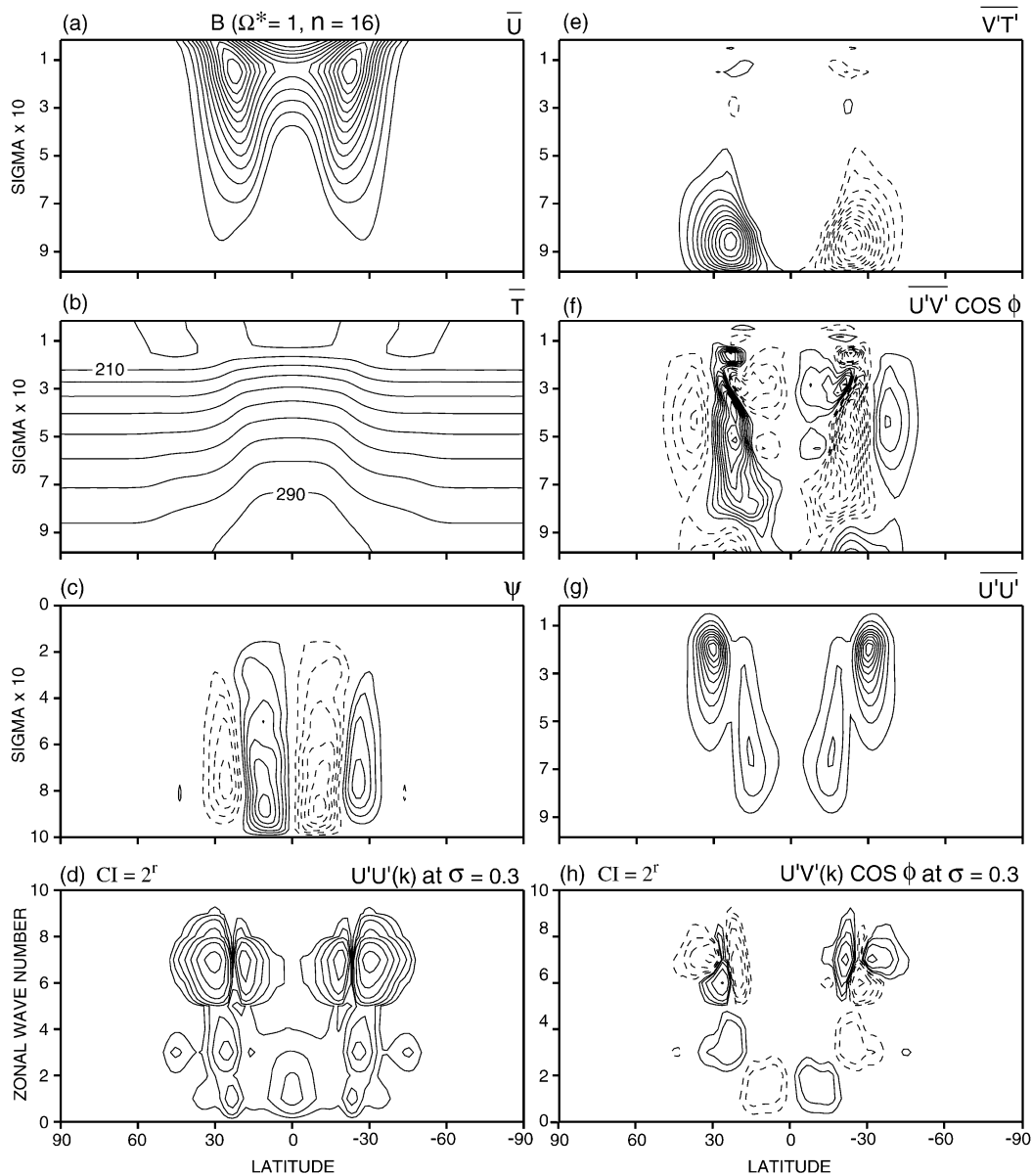
FIG. 5. Meridional sections of the primary mean and eddy fields for the superrotating B solution with $\Omega^* = 1$ and $n = 16$. The contour intervals are (a) 5 m s^{-1}, (b) 10 K, (c) 0.015 s^{-1}, (e) 1 K m s^{-1}, (f) 1 m^2 s^{-2}, and (g) 25 m^2 s^{-2}. To display weaker values near the equator, the contour values in the spectral plots are spaced in powers of two, as (d) 2^r m^2 s^{-2}, $r = (1, 2, \ldots, 7)$ and (h) $\pm 0.5 \times 2^r$ m^2 s^{-2}, $r = (0, 1, \ldots, 4)$. The spectra are evaluated at $\sigma = 0.3$. The zero-value contours are omitted. Labels and negative contours as in Fig. 3.

late the particular process that determines the equatorial westerly.

c. The stratospheric effect

The flatter $\overline{u}(\phi)$ profile seen at low rotation rates raises a question as to what factors, other than Ω^*, control the amplitude of the equatorial westerly relative to that of the main jet. The heating parameters Δ and δ can alter the magnitudes of both currents by altering the scale and strength of the underlying instabilities but they

rarely produce a flatter profile. However, another factor—the thickness of the stratosphere relative to the troposphere—does play a significant role in determining the jet profile. Thus, on repeating the B case with T_s set to 175 K to give a thinner 100-mb stratosphere,[7] the W_0 current becomes 25% stronger relative to the W_1 jet, but the eddy fluxes and spectra are essentially unchanged.

Furthermore, other cases show that when the strato-

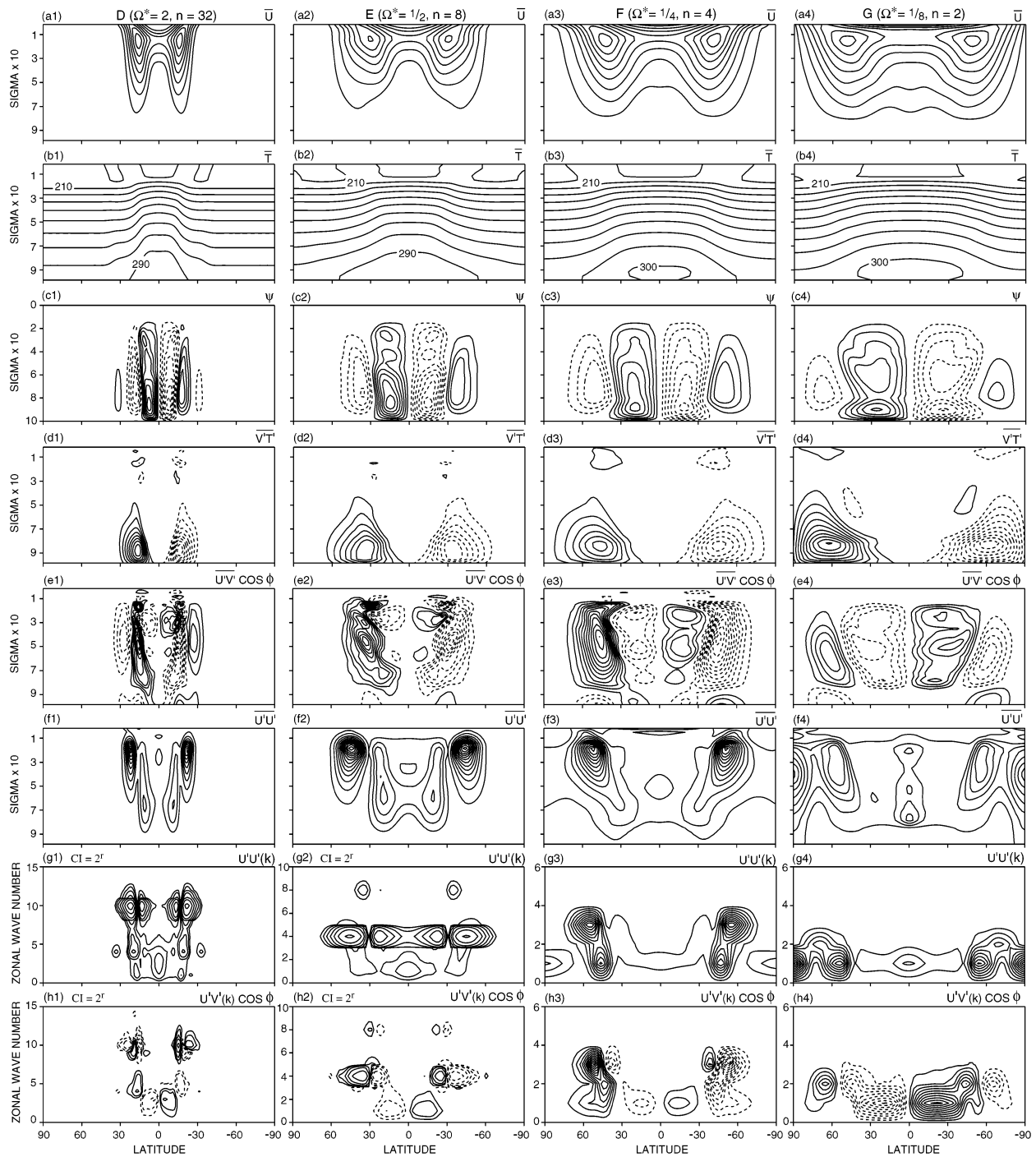[7] The standard value, $T_s = 200$ K, gives a 200-mb layer.

FIG. 6. Meridional sections of the primary mean and eddy fields for the D–G solutions with different rotation rates. The contour intervals are (a1–a4) 8 m s^{-1}, and (b1–b4) 10 K, plus the following: for case D, (c1) 0.01 s^{-1}, (d1) 1 K m s^{-1}, (e1) 1 m^2 s^{-2}, (f1) 25 m^2 s^{-2}, (g1) 2^r m^2 s^{-2}, $r = (1, 2, \ldots, 7)$, and (h1) $\pm 0.5 \times 2^r$ m^2 s^{-2}, $r = (0, 1, \ldots, 4)$; for case E, (c2) 0.02 s^{-1}, (d2) 2 K m s^{-1}, (e2) 2 m^2 s^{-2}, (f2) 25 m^2 s^{-2}, (g2) 5×2^r m^2 s^{-2}, $r = (0, 1, \ldots, 6)$, and (h2) $\pm 2^r$ m^2 s^{-2}, $r = (0, 1, \ldots, 4)$; for case F, (c3) 0.02 s^{-1}, (d3) 2 K m s^{-1}, (e3) 1 m^2 s^{-2}, (f3) 15 m^2 s^{-2}, (g3) 15 m^2 s^{-2}, and (h3) 1 m^2 s^{-2}; for case G, (c4) 0.02 s^{-1}, (d4) 1 K m s^{-1}, (e4) 1 m^2 s^{-2}, (f4) 10 m^2 s^{-2}, (g4) 10 m^2 s^{-2}, and (h4) 0.5 m^2 s^{-2}. The spectra are evaluated at $\sigma = 0.3$. The zero-value contours are omitted. Labels and negative contours as in Fig. 3.
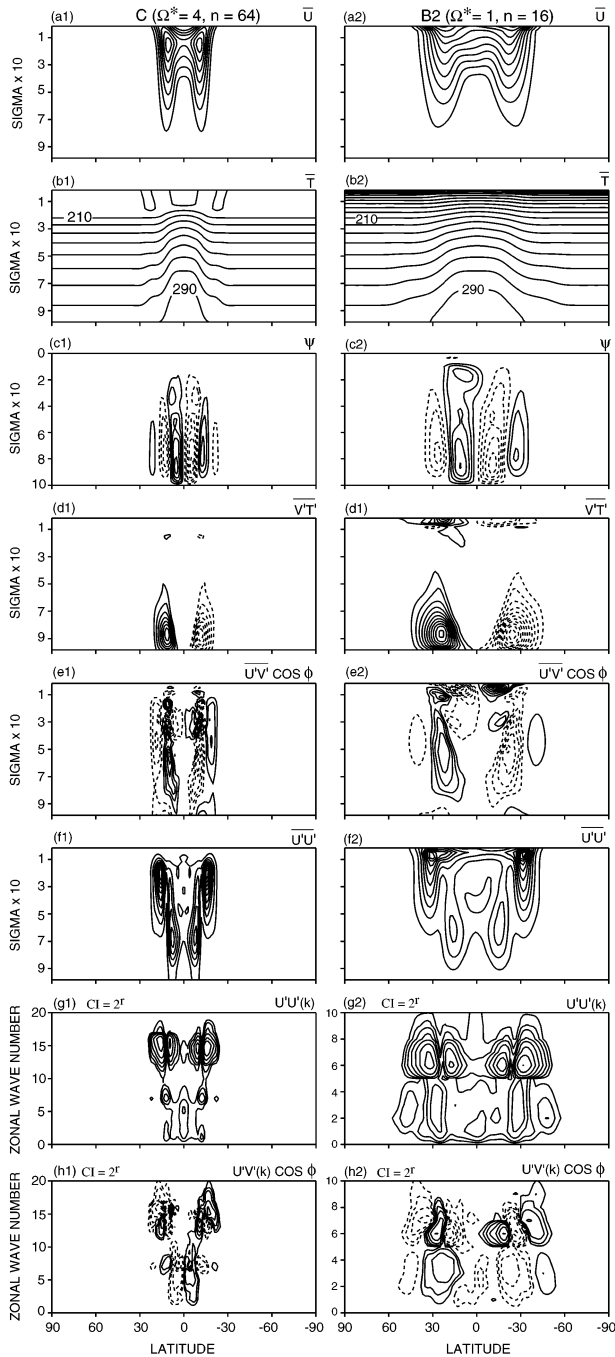
FIG. 7. Meridional sections of the primary mean and eddy fields for the C case with $\Omega^* = 4$, and for the variant B2 case with no stratosphere. The contour intervals are (a1–a2) 8 m s^{-1}, and (b1–b2) 10 K, plus the following: for case C, (c1) 0.01 s^{-1}, (d1) 0.8 K m s^{-1}, (e1) 1 m^2 s^{-2}, (f1) 10 m^2 s^{-2}, (g1) 2^r m^2 s^{-2}, $r = (0, 1, \ldots, 6)$, and (h1) $\pm 0.1 \times 2^r$ m^2 s^{-2}, $r = (0, 1, \ldots, 5)$; for case B2, (c2) 0.02 s^{-1}, (d2) 1 K m s^{-1}, (e2) 2 m^2 s^{-2}, (f2) 20 m^2 s^{-2}, (g2) 2^r m^2 s^{-2}, $r = (0, 1, \ldots, 7)$, and (h2) $\pm 0.2 \times 2^r$ m^2 s^{-2}, $r = (0, 1, \ldots, 6)$. The spectra are evaluated at $\sigma = 0.3$. The zero-value contours are omitted. Labels and negative contours as in Fig. 3.

sphere is completely absent, the ratio of the two currents tends to be closer to unity. One such case, B2 in Fig. 7, illustrates this effect for $\Omega^* = 1$. Omitting the stratosphere in effect eliminates the reversal of the zonal shear that closes the jet contours and reduces the jet amplitude. Thus, the W_0 current approaches the W_1 jet in amplitude (Table 1) and produces a relatively flat flow profile aloft in low latitudes (Fig. 7a2).

This B2 case is also unusual in that the two W_1 jets differ from each other, making the flow profile asymmetric about the equator for lengthy periods of time. This asymmetry is real, not a sampling error, and closely matches that seen in some Jovian wind profiles (cf. Fig. 3 of Williams 1985). Related asymmetries occur in the Hadley cells and the equatorward $\overline{u'v'}$ fluxes, both of which now reach the upper boundary.

Clearly, systems with a thinner or nonexistant stratospheric layer exhibit the usual superrotating flows but also seem to favor a larger W_0 current relative to the W_1 jet. This can result in a flat zonal flow that looks like a simple equatorial jet at any rotation rate.

5. Eliassen–Palm fluxes and potential vorticity gradients

The Eliassen–Palm (EP) diagrams for the various solutions give further insight into how the eddies originate and function in the classical and superrotating flows. The overall E and $\mathbf{F}$ fields are presented in Fig. 8, while Fig. 9 focuses on the weaker low-latitude contributions. In addition, the geostrophic and main ageostrophic components at the equator are illustrated in Fig. 10 for the basic B case. Only in Fig. 8 are the $F^{(\phi)}$ components rescaled (magnified) to expose their form.

According to theory, the E flux divergence provides a measure of the source and magnitude of the transient and irreversible eddy processes, as well as the eddy forcing of the zonal mean circulation, regardless of whether the eddies are linear or nonlinear, wavelike or turbulent. The $\mathbf{F}$ flux vectors give a measure of the wave propagation from one location to another if the eddy dynamics involves planetary waves. If the eddies are turbulent the orientation of the vectors still measures the relative magnitudes of the fluxes of heat and momentum in a meaningful way. However, interpreting the epigrammatic EP diagrams is often difficult, ambiguous, and complicated when the underlying processes are not fully understood (Andrews 1987). For example, although negative (convergent) E regions are expected for linear waves, positive (divergent) values can occur for linear waves that are subject to dissipation by friction or thermal damping. To help resolve these issues, the mean potential vorticity gradients are also calculated.

a. Rotational range of Eliassen–Palm fluxes

The EP diagrams for case A are given in Figs. 8a and 9a to recap the standard interpretation of the classical
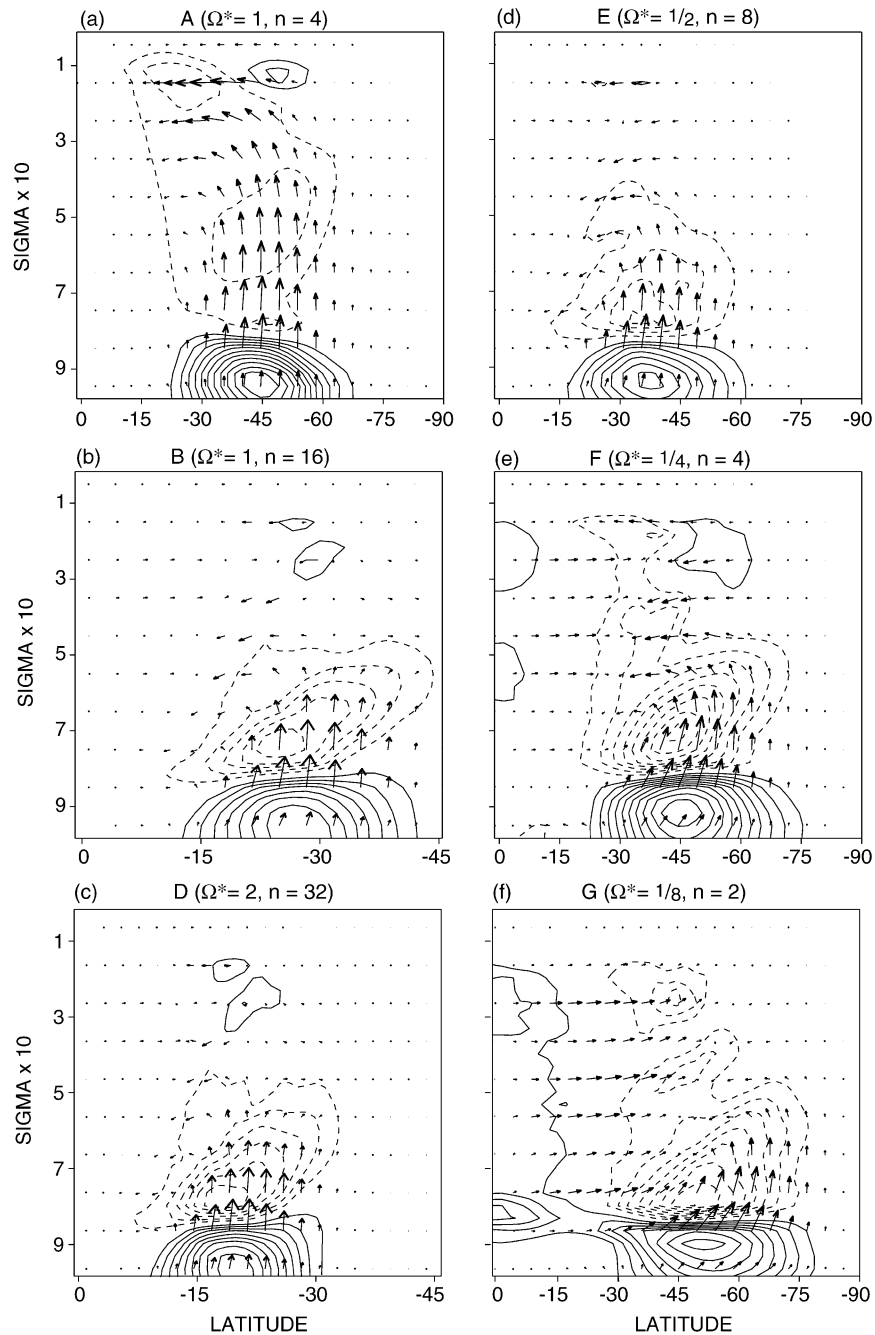
FIG. 8. Meridional sections of the Eliassen–Palm flux divergence E and flux vectors $\mathbf{F}$ for six basic cases with different rotation rates. To expose the latitudinal component, the $F^{(\phi)}$ vector component is magnified by a factor of (a)–(e) 5 and (f) 3. The contour interval for E and the maximum values of $F^{(\phi)}$ and $F^{(p)}$ are, in order, (a) (1.0, 1.7, 1.8), (b) (1.0, 0.2, 1.2), (c) (1.0, 0.2, 1.5), (d) (1.0, 0.4, 1.1), (e) (0.2, 0.2, 0.3), and (f) (0.1, 0.1, 0.1), in units of 10^{-5} m². The zero-value contours are omitted.

regime. As expected, the E and $\mathbf{F}$ fields closely resemble the normal form for a nonlinear baroclinic instability averaged over a complete lifecycle (cf. Edmon et al. 1980). The fields are consistent with a baroclinic instability that arises near the surface in midlatitudes and generates linear waves that propagate vertically across

the convergent E flux region before turning equatorward at the tropopause. These waves transport easterly momentum equatorward, thereby supporting the westerly jet in midlatitudes, before being dissipated in the subtropics. The E flux convergence remains strong aloft, even though the ageostrophic terms of (4)–(6) act to
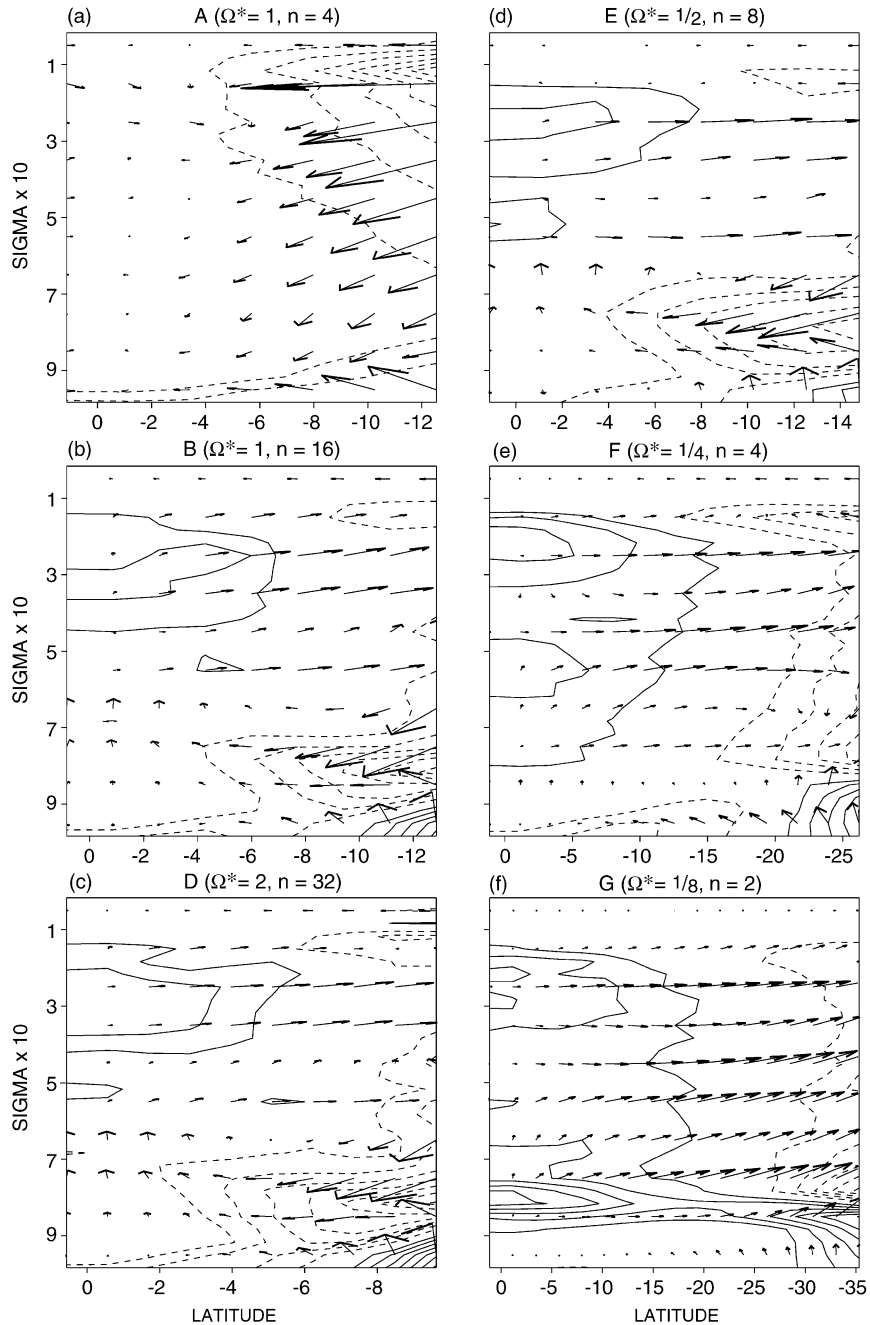
FIG. 9. Low-latitude sections of the Eliassen–Palm flux divergence E and flux vectors $\mathbf{F}$ for six cases with different rotation rates. The contour interval for E and the maximum values of $F^{(\phi)}$ and $F^{(p)}$ are, in order, (a) (2.0, 0.3, 0.3), (b) (2.0, 0.2, 0.7), (c) (2.0, 0.2, 1.0), (d) (2.0, 0.4, 0.7), (e) (1.0, 0.2, 0.5), and (f) (0.8, 0.2, 0.3), in units of 10^{-6} m^2. The zero-value contours are omitted.

reduce it while enhancing the secondary divergent component at the tropopause. Furthermore, according to Fig. 9a, the main flux convergence extends into low latitudes both aloft and near the surface, and the associated vectors imply that the waves propagate downward as well as equatorward to about 6°, albeit weakly.

On the other hand, in the basic superrotating B case,

the main E flux divergence and convergence regions associated with the baroclinic instability and vertical wave propagation are much shallower, lying mainly in the lower half of the troposphere (see Fig. 8b). The main $\mathbf{F}$ flux vectors are upward with a slight poleward tilt, before turning equatorward at midheight and then gradually descending into the subtropics. In low latitudes,
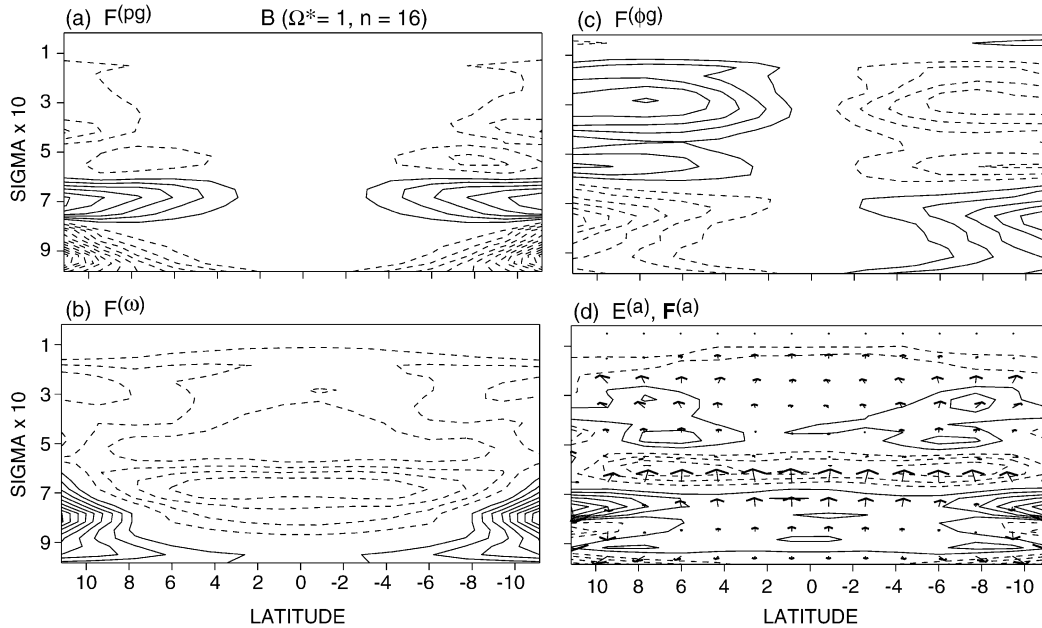
FIG. 10. Meridional sections of the main geostrophic and ageostrophic components of the Eliassen–Palm fields near the equator, for the basic B case with $\Omega^* = 1$ and $n = 16$. The contour intervals are (a) 5×10^{-3} for $F^{(pg)}$, (b) 5×10^{-3} for $F^{(\omega)}$, (c) 1×10^{-7} for $F^{(\phi g)}$, and (d) 7×10^{-7} for $E^{(a)}$, in units of m². The items in (a) and (b) are divided by 10^5 (a pascal) when forming $E^{(a)}$ in (d), where the maximum vector component values of $F^{(\phi a)}$ and $F^{(pa)}$ are 0.3 and 3.5, respectively (10^{-7} m²). The zero-value contours are omitted.

however, the EP fluxes are quite different from the classical ones, as is to be expected (Fig. 9b). A significant divergent E flux forms over the equator in the upper troposphere in keeping with the eddy forcing of the W_0 current. If the dynamics are wavelike, then the $\mathbf{F}$ flux vectors are consistent with the action of a tropical instability that generates the large-scale waves (Fig. 5h) that extend aloft from the equator to about 15° latitude.

To analyze further the EP fields of the B case, the geostrophic and main ageostrophic $\mathbf{F}$ components in low latitudes, along with the net ageostrophic $E^{(a)}$ and $\mathbf{F}^{(a)}$ fields, are plotted in Fig. 10. These show that the $F^{(\phi g)}$ and $F^{(\omega)}$ flux components prevail over $|\phi| < 10°$, with

FIG. 11. Cospectrum of the u' and ω' fields at the $\sigma = 0.7$ level for the B case. The contour values are 2^r for $r = (1, \ldots, 6)$ plus -2^r for $r = (1, \ldots, 8)$, in units of 10^{-3} m² s⁻². The zero-value contours are omitted.

the latter dominating the $E^{(a)}$ convergence zone to give an upward eddy flux at the $\sigma = 0.7$ level. Such an upward transport of easterly momentum is consistent with the action of planetary waves and could tie in with the poleward transport of easterly momentum by the main eddies generated aloft by a tropical instability, given that the vertical flux has a peak at the same large scales, according to the $u'\omega'(k)$ cospectrum in Fig. 11.

At other rotation rates, the EP fields are essentially the same as in the basic B case. Minor differences occur with decreasing Ω^* as the center of the baroclinic instability moves poleward and the lateral eddy scale increases. However, when Ω^* drops to 1/4 and 1/8, the low-latitude and midlatitude EP fluxes start to approach each other in strength, with the main E flux convergence becoming strong again at the tropopause (Figs. 8e,f). According to the $\mathbf{F}$ vectors, the eddies transfer easterly momentum from the equator to near the jet core at 30° and 45° in these two cases (Figs. 9e,f). The E field at $\Omega^* = 1/8$ also contains a unique divergence region that coincides with the uniquely poleward $\mathbf{F}$ vectors at low levels over the equator.

The G case for $\Omega^* = 1/8$ provides an interesting variation on any scenario and is either an exceptional state or a limiting state that contains further clues as to what process produces the W_0 current in the other cases. In the G case, $\mathbf{F}$ is essentially poleward in $|\phi| < 40°$ and upward in $|\phi| > 40°$. Its eddies are dominated by just two modes: $k = 1$ and 2 in Fig. 6h4, which are too large to propagate either poleward or equatorward. This
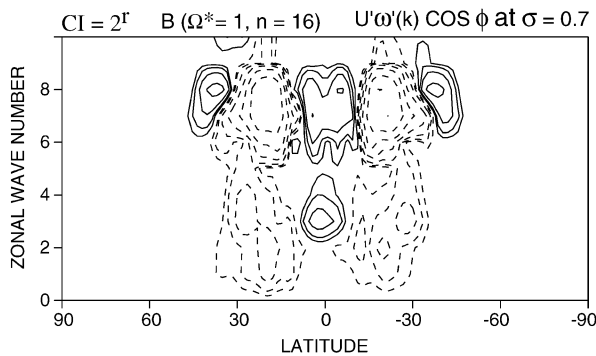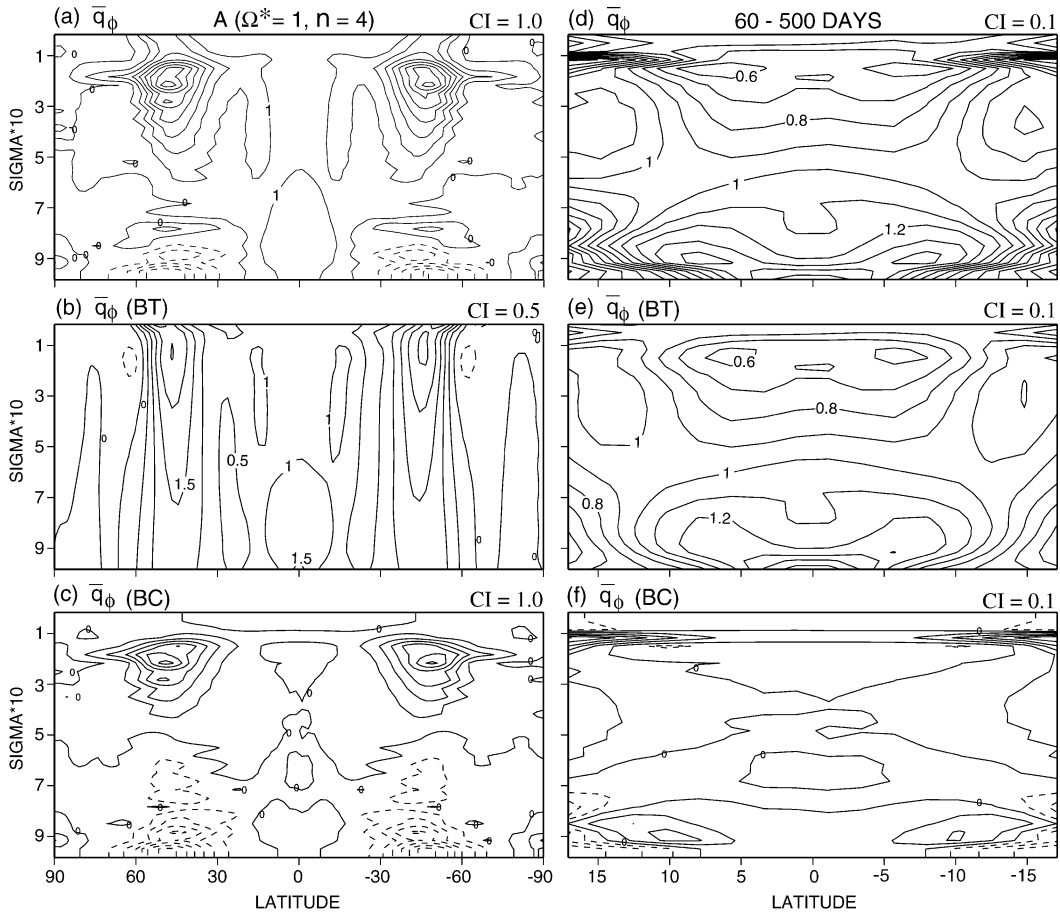
FIG. 12. For the classical A solution, meridional sections of the normalized quasigeostrophic potential vorticity gradient and its barotropic (BT) and baroclinic (BC) components, as defined in (7). All gradients are averaged over the 60–500-day interval and are shown for both (left column) midlatitudes and with smaller contour intervals (CI) for (right column) low latitudes.

suggests that, when the instabilities are of hemispheric scale, the system may only be able to activate modes that transfer easterly momentum poleward. Such behavior would be consistent with the complete exclusion of the classical regime at the lowest rotation rates (Fig. 2).

Thus, there appear to be two fundamental forms of EP flux in the superrotating regime: (a) the basic type as represented by the B solution at $\Omega^* = 1$, where the baroclinic instability dominates the tropical instability; and (b) the limiting type for the hemispheric-scale eddies found at $\Omega^* = 1/8$, where the baroclinic and tropical instability are comparable. Overall, there appears to be a continuity of form as the eddy scale changes with Ω^*, with the $\overline{u'v'}$ flux always converging on the equator for the largest-scale eddies.

b. Regime potential vorticity gradients

To identify the sources of the eddies, we examine the mean quasigeostrophic potential vorticity gradient $\overline{q}_\phi$ and its components as defined in (7). Although the qua-

sigeostrophic approximation is less accurate in low latitudes, the diagnostic remains useful as the barotropic component and planetary wave fluxes dominate near the equator. We recall that the equation for the eddy potential enstrophy on a quasigeostrophic beta plane with lateral coordinate y may be written as

$$\frac{1}{2}\overline{(q'^2)}_t + (\boldsymbol{\nabla} \cdot \mathbf{F})\overline{q}_y = \overline{S'q'}, \qquad (8)$$

where $E = \nabla \cdot \mathbf{F} = \overline{v'q'}$, and S represents the nonconservative processes. Wave sources (instabilities) are expected to occur where $\overline{q}_y$ has the opposite sign to E.

For the classical A solution in midlatitudes, the $\overline{q}_\phi$ field in Fig. 12a is dominated by the baroclinic component and has the opposite sign to the E field at all heights, in keeping with the existence of a baroclinic instability at the ground. In the Tropics ($|\phi| \leq 15°$), however, $\overline{q}_\phi$ is positive everywhere at all times because of the predominant beta component, so the region lacks any indigenous eddy sources.

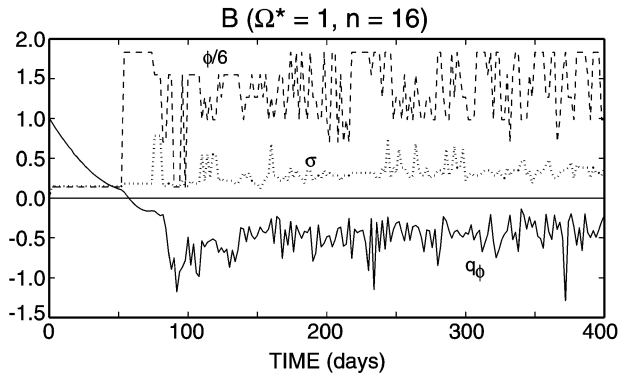But in the superrotating B solution, the $\overline{q}_\phi$ field al-

FIG. 13. For the superrotating B solution, transients of the minimum values of the normalized potential vorticity gradient, as defined by (7), and their vertical and normalized latitudinal locations in the free tropical region, as defined by $|\phi| \leq 12°$ and $\sigma \leq \sigma_b$.

ways has negative values in the Tropics according to the transients of the minimum values (Fig. 13). These minima mostly occur near the tropopause ($\sigma = 0.2$) but occasionally at depth ($\sigma = 0.6$) and fluctuate in latitude between 6° and 12°, after leaving the equator following the rapid W_0 growth phase. Note, however, that because the negative transients change location, the time-mean $\overline{q}_\phi$ may not exhibit any significant negative values. This becomes clearer when the time means are plotted separately for the W_0 growth phase (Fig. 14) and for the equilibration phase (Fig. 15).

Consider first the gradients in the subtropics and midlatitudes in Figs. 14a–c and 15a–c. There are two regions with a strong $\overline{q}_\phi$, one centered at $\phi = 20°$, another at $\phi = 45°$, with both associated with the baroclinic instability and consistent with the eddy fluxes of Fig. 5. The source at 20° is made up of contributions from both the barotropic and baroclinic components of $\overline{q}_\phi$, whereas the source at 45° is primarily baroclinic. Little difference exists between the gradients of the growth and equilibration phases in these latitudes as the baroclinic
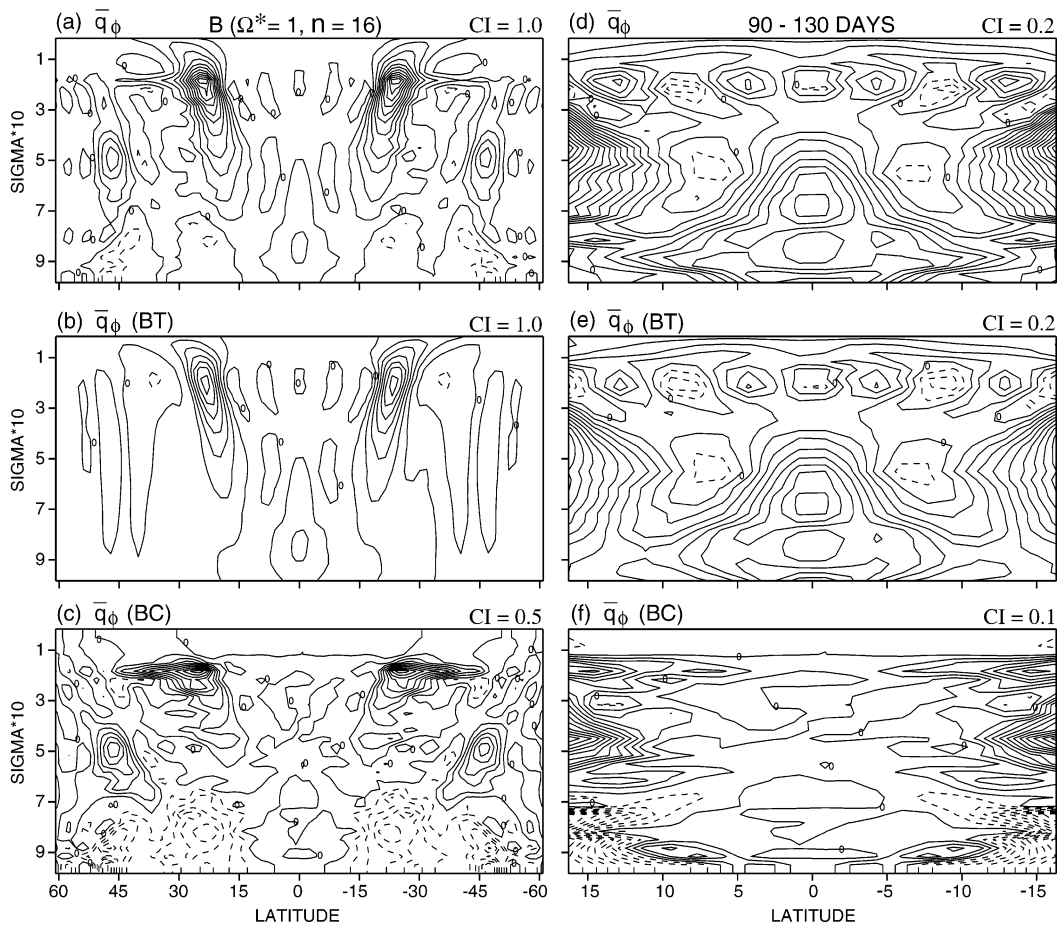

FIG. 14. For the superrotating B solution over the W_0 onset phase, meridional sections of the normalized quasi-geostrophic potential vorticity gradient and its barotropic (BT) and baroclinic (BC) components, as defined in (7). All gradients are averaged over the 90–130-day interval and are shown for both (left column) midlatitudes and with smaller contour intervals (CI) for (right column) low latitudes.
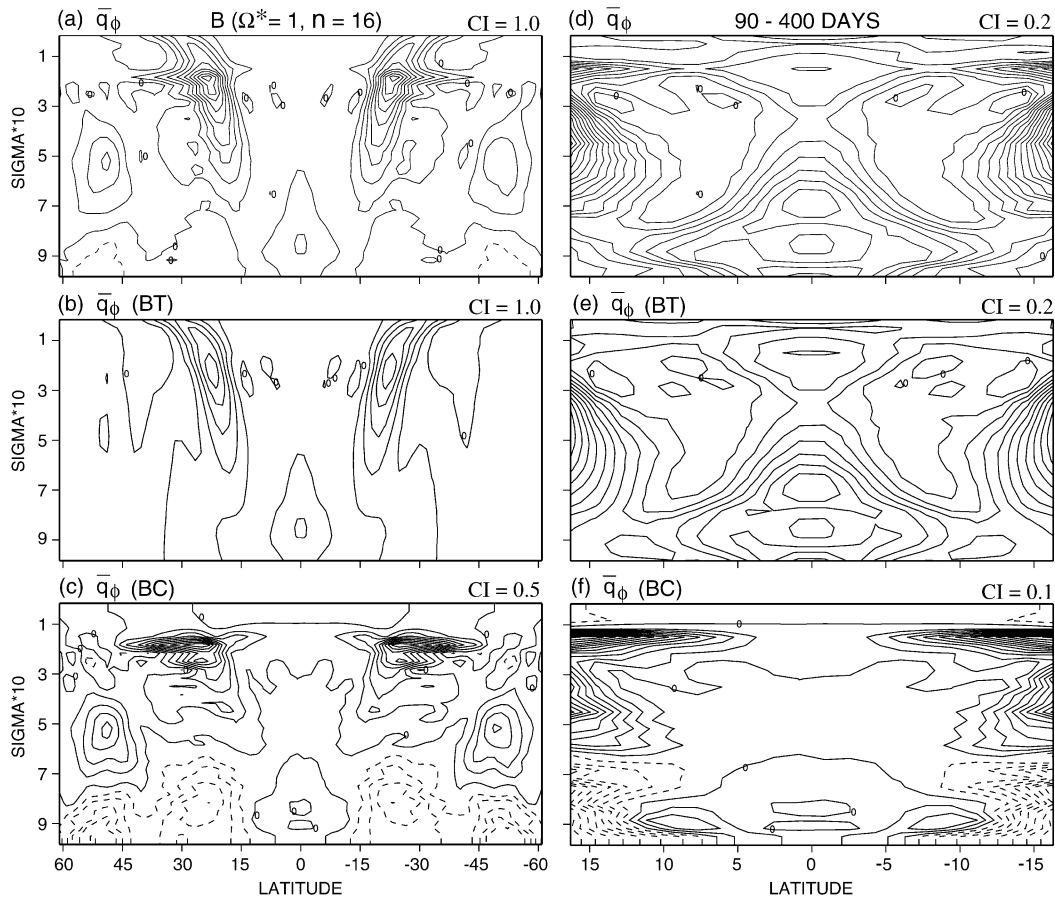
Fig. 15. For the superrotating B solution over the W_0 equilibration phase, meridional sections of the normalized quasigeostrophic potential vorticity gradient and its barotropic (BT) and baroclinic (BC) components, as defined in (7). All gradients are averaged over the 90–400-day interval and are shown for both (left column) midlatitudes and with smaller contour intervals (CI) for (right column) low latitudes.

instability is primarily associated with the poleward half of the jet.

But this is not true of the Tropics, where the smaller contour intervals reveal that during the W_0 growth phase significant areas of negative $\overline{q}_\phi$ exist (Figs. 14d,e). These occur at midheight and near the tropopause and are clearly due to the barotropic component. They also coincide with positive values of the E field. This implies that the eddies producing the superrotation are due to the barotropic instability of the equatorward flank of the W_1 jet.

As the W_0 current equilibrates, a large region of uniform $\overline{q}_\phi$ forms between 5° and 15° with gradients close to zero and with patches of negative values aloft (Figs. 15d,e). This suggests that the eddies act to mix the flow in such a way that the barotropic instability eventually becomes weaker and excluded from the equator, though enough eddy activity remains to maintain the superrotation. The W_0 flow equilibrates in effect by reducing the extent of the region with negative $\overline{q}_\phi$.

Overall, the diagnostics suggests that the W_0 current is created and maintained by the tropical barotropic in-

stability of the W_1 jet. This weak barotropic instability coexists with the strong extratropical baroclinic instability. At lower rotation rates these two instabilities are equally influential, with the result that W_0 approaches W_1 in amplitude.

6. Conclusions

By changing the value of one parameter, n, which defines the location of the baroclinic zone, it is possible to change the circulation regime and the climate in the model atmosphere. At the normal rotation rate, when the center of the baroclinic zone lies poleward of 30° (for $n \le 4$), the classical regime prevails. Then, as it moves equatorward of 30° (for $n = 6$–12), equatorial westerlies with $W_0 \ll W_1$ arise but eventually collapse, thus making their state transitory. Only when the center lies equatorward of 20° (for $n \ge 16$) does the superrotating regime prevail. The equatorial W_0 current can even approach the main W_1 jet in amplitude, particularly when the stratosphere is thin relative to the troposphere or when the rotation rate is low; then the flow displays

what looks like a single jet at the equator. Given that the initial axisymmetric jets lie close to 30° for both the classical A case and the superrotating B case, the evolution into radically different circulations indicates that this model atmosphere too is capable of a bifurcation of the form proposed by Suarez and Duffy (1992).

The superrotating regime exists for all rotation rates that allow baroclinic and barotropic instabilities and it persists robustly for heating forms that vary as $n = (2, 4, 8, 16, 32, 64)$ when $\Omega^* = (1/8, 1/4, 1/2, 1, 2, 4)$, respectively. Thus the regime prevails when the center of the baroclinic zone lies at a latitude on or below the lower curve shown in Fig. 2—at least for the parameters selected. In most cases, the eddy fluxes that drive the equatorial current are created by the action of the largest-scale modes; and these, in turn, are probably generated by the barotropic instability of the equatorward flank of the low-latitude jet. They could also be associated with horizontal nonlinear interactions involving the medium scale waves created by the baroclinic instabilities, or by vertical interactions involving waves that propagate into low latitudes near the surface before turning upward at the equator, but this is less likely.

The superrotating states discussed by Suarez and Duffy (1992) and by Saravanan (1993) appear to be related to those presented here though the sources of the large-scale eddies that drive the equatorial westerlies differ. Their heating arrangement, however, may stand more of a chance of occurring in the existing terrestrial atmosphere than does our simpler but more extreme form, one that requires the baroclinicity to have a strong component in low latitudes. But at low rotation rates, superrotation is the natural state for most systems, including GCMs with standard terrestrial heating arrangements (Williams 1988).

Nevertheless, the existence of the superrotating regime implies that the earth and other planets could have additional climate modes, although their actual realization may be rare. For the earth, the equatorial westerly is more likely to occur simultaneously with the midlatitude regime, under a heating with the hybrid form $P = c_2 \cos^2 \phi + c_{16} \cos^{16} \phi$, where c_2 and c_{16} are constants[8] of order one. Such a distribution would be similar

to the one used in early dry GCM studies to allow for condensation effects near the equator [see Fig. A5 of Smagorinsky (1963)]. Equatorial jets could also occur on the Jovian planets under related processes, according to the recent modeling of circulations in vertically confined layers (discussed in a separate paper). The terrestrial superrotating regime provides a basis for understanding the equatorial jet of any planet, as well as providing a measure of the stability of the earth's climate.

REFERENCES

Andrews, D. G., 1987: On the interpretation of the Eliassen–Palm flux divergence. *Quart. J. Roy. Meteor. Soc.,* **113,** 323–338.

——, and M. E. McIntyre, 1978: Generalized Eliassen–Palm and Charney–Drazin theorems for waves on axisymmetric mean flows in compressible atmospheres. *J. Atmos. Sci.,* **35,** 175–185.

Bourke, W., 1974: A multi-level spectral model. I. Formulation and hemispheric integrations. *Mon. Wea. Rev.,* **102,** 687–701.

Edmon, H. J., B. J. Hoskins, and M. E. McIntyre, 1980: Eliassen–Palm cross sections for the troposphere. *J. Atmos. Sci.,* **37,** 2600–2616.

Gordon, C. T., and W. F. Stern, 1982: A description of the GFDL global spectral model. *Mon. Wea. Rev.,* **110,** 625–644.

Held, I. M., and B. J. Hoskins, 1985: Large-scale eddies and the general circulation of the troposphere. *Advances in Geophysics,* Vol. 28A, Academic Press, 3–31.

——, and M. J. Suarez, 1994: A proposal for the intercomparison of dynamical cores of atmospheric general circulation models. *Bull. Amer. Meteor. Soc.,* **75,** 1825–1830.

Peixoto, J. P., and A. H. Oort, 1992: *Physics of Climate.* American Institute of Physics, 520 pp.

Saravanan, R., 1993: Equatorial superrotation and maintenance of the general circulation in two-level models. *J. Atmos. Sci.,* **50,** 1211–1227.

Smagorinsky, J., 1963: General circulation experiments with the primitive equations. I. The basic experiment. *Mon. Wea. Rev.,* **91,** 99–164.

Suarez, M. J., and D. G. Duffy, 1992: Terrestrial superrotation: A bifurcation of the general circulation. *J. Atmos. Sci.,* **49,** 1541–1554.

Williams, G. P., 1985: Jovian and comparative atmospheric modeling. *Advances in Geophysics,* Vol. 28A, Academic Press, 381–429.

——, 1988: The dynamical range of global circulations—I. *Climate Dyn.,* **2,** 205–260.

[8] Alternatively, c_{16} can be made a function of longitude to reproduce the tropical wave forcing.